Present design of the Steering Mirror Assembly (SMA) for ITER ECHUL

A. Xydou[a,*], R. Chavan[a], T. Goodman[a], S. Julia Torres[b], C. Marraco Borderas[a], A. Mas Sanchez[a], H. Torreblanca Quiroz[a]

[a]*Ecole Polytechnique Fédérale de Lausanne (EPFL), Swiss Plasma Center (SPC), CH-1015 Lausanne, Switzerland.*
[b]*Fusion for Energy, Josep Pla 2, Torres Diagonal Litoral B3, E-08019 Barcelona, Spain.*

Abstract

In the ITER Tokamak, four Electron Cyclotron Heating Upper Launchers (ECHUL) are needed to control plasma instabilities at the rational surfaces, most importantly the q=3/2 and q=2/1 neoclassical tearing modes (NTMs). Each ECHUL is equipped with a set of fixed mirrors (M1, M2 and M3) and a front steering mirror set (M4). The millimetre waves are reflected from these mirrors. EC beams are grouped in two rows of four beams each. There are two M4 mirrors, called Upper and Lower Steering Mirror Assemblies, that rotate independently to target the locations of the instabilities in real time.

The previous design of M4 showed no compliance of the non-actively cooled components like bellows and springs after including the thermal load of the mm-wave stray radiation and direct plasma radiation. This paper reports the main design changes with the objective to reduce the thermal loads on the non actively cooled components. The Upper Steering Mirror Assembly (USMA) is presented here as an enveloping case. The components structural integrity enforcing the ITER Structural Design Code for the In-Vessel Components (SDC-IC) is assessed by finite elements analyses.

1. Introduction and background

The upper and equatorial port launchers constitute the torus antenna parts of the electron cyclotron heating and current drive (EC H&CD) system

*Corresponding author
Email address: anastasia.xydou@epfl.ch (A. Xydou)

of ITER.

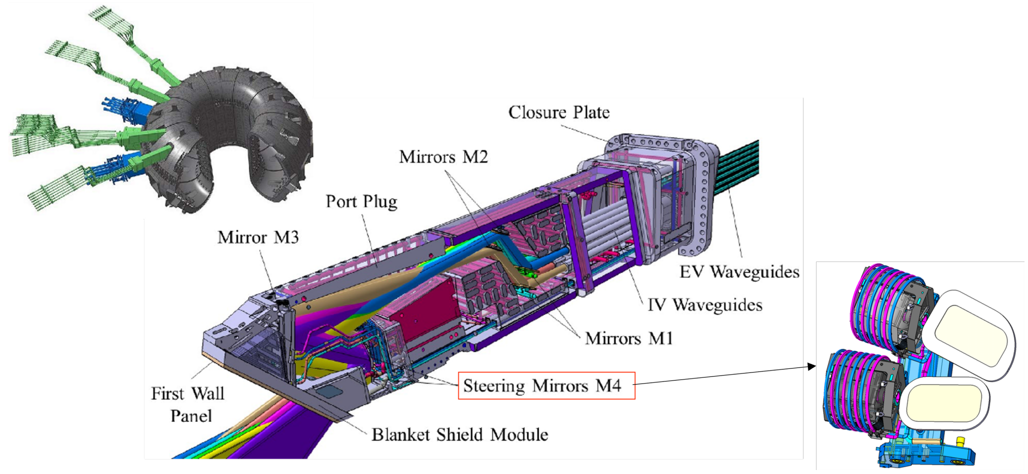

Figure 1: The ITER ports 12, 13, 15 and 16 are attributed to the upper launchers, with the antenna system in port 16 being installed for the first plasma (FP) operational phase. The vertical section illustrates the main elements of the mm-wave transmission system within the upper port plug, with the steering mirrors M4 (previous design) placed in the front part, protected by the blanket shield module (BSM). For visibility, the eight beams are represented individually as solid, color coded objects.

The EC system operates at a frequency of 170 GHz and each gyrotron supplies a beam with the nominal power of 1 MW at the diamond window in the end of the transmission line in the port cell. The four upper launchers (UL) designed for the ITER EC system are described as front steering (FS) type systems, in which the beams are reflected and accurately directed by a set of plasma facing movable mirrors towards precisely localised regions in the plasma. The current launcher configuration uses two steering mirror assemblies (SMA) in each port plug transmitting eight beams, thus reflecting four, partially overlapping beams (in toroidal direction) on each steering mirror. The positions of the upper launchers relative to the torus and the mm-wave system within the port plug are illustrated in Fig. 1.

EPFL-SPC proposed the steering mechanism concept in 2005 [1]. Since then the design has evolved [2] concurrently with the ITER design requirements. In [3] the optimisation of the mirror's back plate cooling circuit to handle the Vertical Displacement Event (VDE) loads was presented. After that, by considering the combination of mm-wave stray radiation, plasma and nuclear heating, the former M4 design (see Fig. 1 right corner) showed problems on the components not equipped with a cooling system (springs, bellows, flexural pivots). Specifically high temperatures were reached in springs and bellows, mostly due to stray radiation, and nuclear heating. Flexural pivots were also overheated by stray radiation too. The structural integrity performed on the flexural pivots (made of Titanium alloy) showed the maximum stresses exceeding by 12 % the allowable.

This paper presents the redesign activity of the steering mirror assembly (SMA) aiming to reduce the temperature of M4 internal components during operation. The Normal Operation (NO) scenario is examined as load case scenario category I and the resulting stress values are compared to the material limits provided by the SDC-IC [4, 5] code.

2. Design description

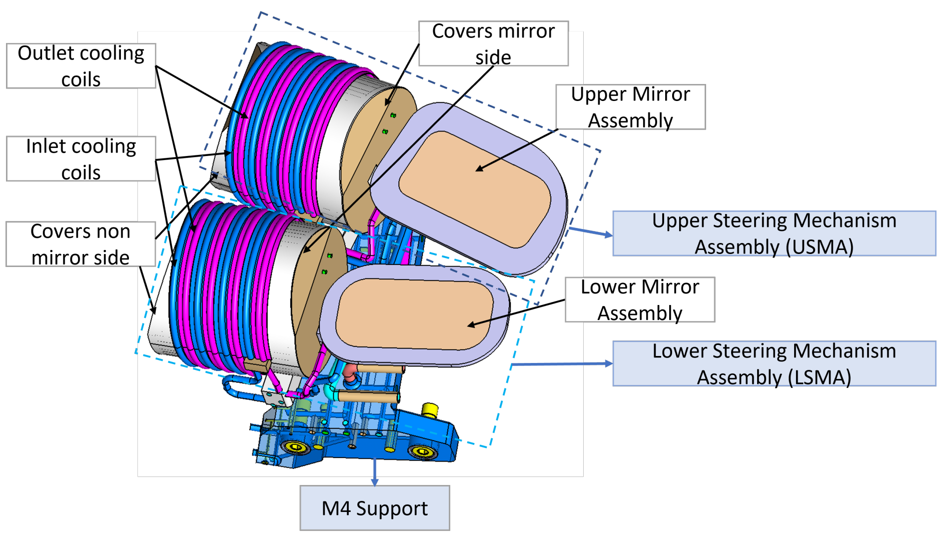

Figure 2: Current M4 design.

The M4 actuating system is composed of two steering mechanisms which are nearly identical (Fig. 2), small differences apply due to the space reservations. The USMA and LSMA are pre-assembled on the M4 support before their insertion into the EC UL Port Plug [6].

Each mechanism is based on four, pressure-controlled, pneumatically-actuated bellows working against six, helicoidally-machined, preloaded compressive springs (Fig. 3). The ends of the bellows are welded to the stator

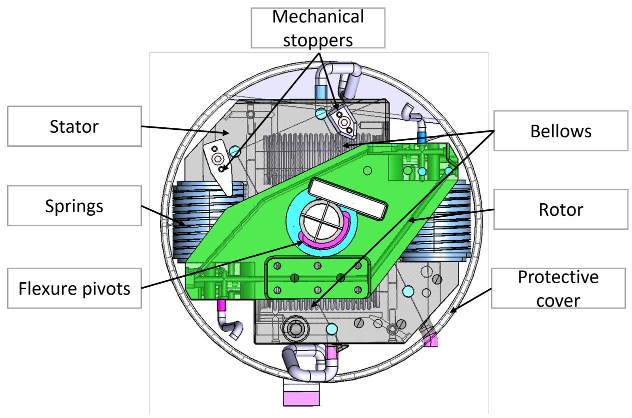

Figure 3: Upper/Lower steering mechanism detailed axial view after hiding the protective cover on the mirror side.

(fixed component) and the rotor (moving component). One side of the springs is welded to the stator and the other side is welded to the rotor. This system allows the mirror (attached to the rotor by bolted connection) to rotate around the axes of two flexure pivots. This arrangement offers 1 DOF (degree of freedom, rotation around the flexure pivot axis), all other DOFs are blocked.

The stator is the main 'central part' of the M4 SMA as it supports the reflective mirror that is attached to the rotor and provides the fixation point for the compressive springs and the pneumatic housing for the bellows. Two helical cooling pipes (one for the incoming and another for the outgoing circuit) are used to feed the PHTS (Primary Heat Transfer System) cooling water into the moving parts of each mechanism. The water is fed in parallel to the USMA and LSMA through each stator. Subsequently, all components are then cooled in series. Thus, the allocated cooling mass flow rate is determined by the flow required to cool the reflective steering mirror; the bellows, springs and pivots are the only passively cooled components in the assembly.

The implementation of water channels within the springs and pivots would require the additive manufacturing method which is not accepted for the manufacturing of the in-vessel components. Concerning the bellows which are directly welded on the stator and pressurized externally with liquid Helium, there is not an evident way to directly cool them. Therefore, the proposed solution -shown here in Fig. 2- includes:

- The maximisation of heat conduction at the component interfaces.

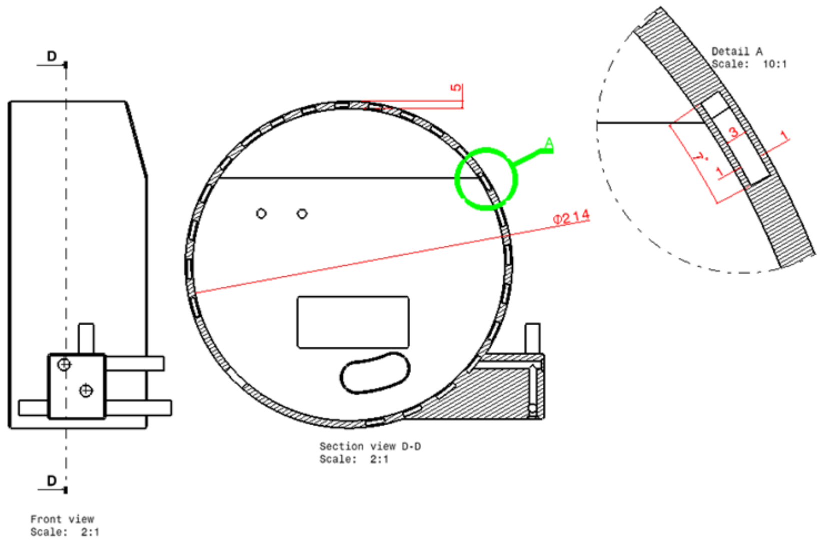

Figure 4: Detailed view of the cooling channels in the cap fixed to the rotor. The channels in the caps fixed to the stator follow the same principle.

- The addition of a protective cover over each steering mechanism. The protective covers are actively cooled components which provide shielding against plasma heat and mm-wave stray radiation.

- The cooling coils which route the water from the stators to moving components are now equipped with 'wings' to reduce leakage of mm-wave stray radiation through gaps.

The covers, due to their small mass, do not contribute to neutron shielding. The heat load generated by the neutrons within the internal components (bellows, springs, flexure pivots) is low compared to plasma and stray radiation loads. This heat will be extracted mainly by conduction through the solid contacts with the water-cooled stator and rotor.

Both USMA and LSMA have two covers. One is fixed to the rotor, and one is fixed to the stator. Fig. 4 presents a detailed view of water channels on the protective covers.

The water scheme has been modified to accommodate the design changes. The cooling circuit consists of two independent parts which receive the same mass flow of 0.25 kg/s, at the same inlet temperature of 75 °C. A schematic representation is shown in Fig. 5.

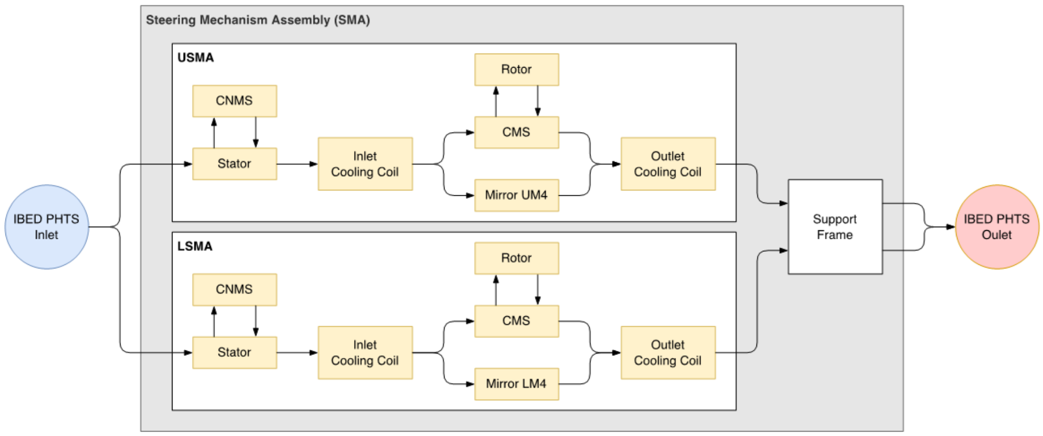

Figure 5: Schematic representation of the cooling circuit. CNMS stands for Cover Non Mirror Side and CMS stands for Cover Mirror Side.

Both upper and lower stators are fed with water in parallel. Each stator provides water to the cover (CNMS) which is fixed to it as a bypass. A collector is part of the cover which is fixed to the rotor (CMS). The water from the inlet coil is split between the cover which is fixed to the rotor and the mirror support plate. Water is bypassed from the cover to feed the rotor. Both outlet cooling coils provide water to the M4 Support.

The cylindrical part of the protective covers is made of Alloy 660 and the flat part is made of CuCr1Zr. The CuCr1Zr is shown with orange colour in Fig. 2. The material choices were made based on the understanding that in-vessel PHTS pressurized components manufactured by additive methods are not (yet) approved in ITER. Furthermore, the current design avoids cooling channels interfering with welded interfaces. Thus, by using CuCr1Zr for the flat end parts with no cooling channels, the cooling performance is improved. Stainless steel 316LN was the initial candidate for the cylindrical parts but the primary stresses due to the water pressure were exceeding that material's limits. Fig. 6 highlights the different materials of the SMA components. In the thermal-hydraulic analysis the thermal properties are considered functions of temperature [7].

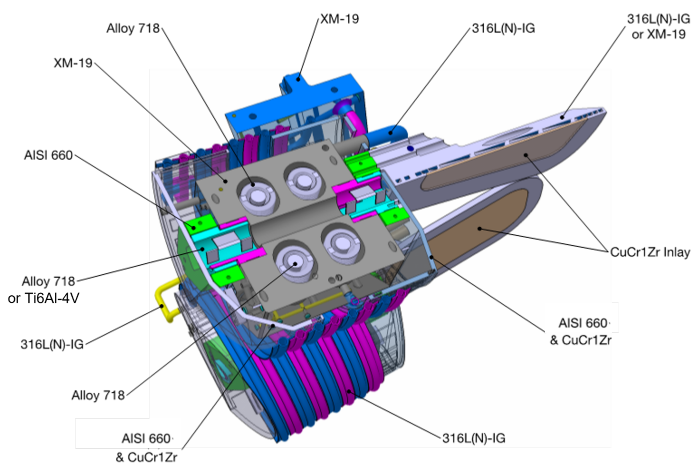

Figure 6: Materials of the SMA. The springs, which are not shown in this cut-view, are made of Alloy 718.

3. Finite element analyses

The USMA should comply with the stringiest requirements and in particular with load cases which belong to Categories I and II as the Operational Loading Conditions and Likely Loading Conditions, respectively.

As a first step, the USMA is analysed against the NO loads (normal plasma operation) with a steady-state CFD conjugated heat transfer analysis which is performed in ANSYS Workbench 2021 R2 CFX to assess the flow distribution and heat transfer taking place in the updated design of the M4. Next, the temperature results are extracted and mapped on the several components in the mechanical solver, together with the mechanical loads (water pressure, helium pressure and gravity) of the NO scenario. The mechanical simulation is a linear simulation. A stress integrity assessment is performed on the critical components according to the design limits and a fatigue check is applied on the flexure pivots.

In a following step, the Vertical Displacement Event (VDE) III is calculated using ANSYS Maxwell. This analysis aims only to compare the induced forces and moments at the pivot location with the protective covers made of two materials CuCr1Zr and Alloy 660, and with protective covers made entirely of Alloy 660.

3.1. Normal Operation scenario

3.1.1. Geometry

Fig. 7 presents the USMA design used for the NO scenario calculation. The water volume used in the thermal hydraulic analysis is highlighted in blue. The geometry of the bellows and pivots has been simplified to reduce the number of elements. Several chamfers and holes have been deleted.

In the mechanical solver the real geometry of the pivots is considered without any simplifications. Nevertheless, due to CPU limitations, springs and bellows have been replaced with spring elements with stiffness equal to 18.8 and 10.5 N/mm, respectively.

Tetrahedral elements are used for the mesh in both thermal-hydraulic and mechanical simulations of the USMA.

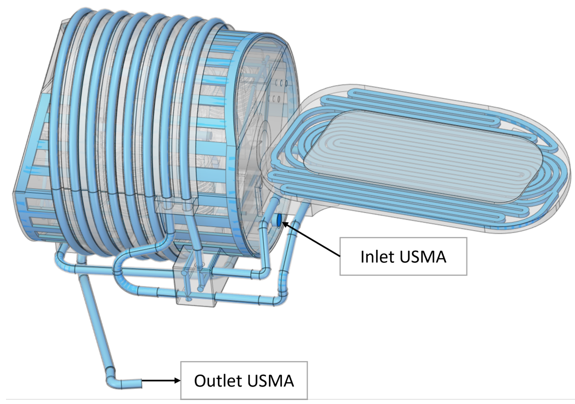

Figure 7: USMA geometry used in the NO scenario.

In the thermal-hydraulic model the element size of the water volume is 1 mm. Due to the size and complexity of the model, no inflation layers are considered for the mesh generation. This approach is followed not only to reduce the number of nodes but also to improve the quality of the mesh. The shear stress transport (SST) kω turbulence model formulation was used.

3.1.2. Boundary conditions

The SMA thermal loading conditions are a function of the various plasma scenarios occurring in the tokamak and the mm-wave exposure. The known thermal loads which are applied in the thermal hydraulic analysis are listed here:

- mm-wave operation (ohmic heating from beam reflection) and stray radiation,
- Plasma radiation,
- Neutronic heating.

Table 1 summarizes the thermal loads applied on the several components except for the ohmic heating. Appendix 6 presents the details of the applied thermal loads. PHTS cooling water with a mass flow of 0.25 kg/s at 75 °C and 4.4 MPa are applied at the inlet of USMA.

The structural part of the analysis uses the following BCs:

- Fixed face on the stator and on the outlet coil face where they are attached to the M4 support;
- Gravitational load;
- Gauge pressure of 4.4 MPa is applied to the cooling channel walls;
- Helium pressure of 2 MPa is applied to the cavities of the stator where the bellows are located;
- Rotation of $\pm 7^\circ$;
- Temperature fields coming from the thermal-hydraulic analysis, with an initial temperature of 75 °C (inlet temperature of the cooling water).

Table 1: Summary of the thermal loads applied on the USMA components at the thermal-hydraulic analyses as well as the materials.

Component	**Material**	**Nuclear heating (W)**	**Plasma heating (W)**	**mm-wave stray radiation (W)**
Stator	XM19	961.6	0	0
Spring	Alloy 718	24.7	0	0
Bellow		17.6	0	0
Flexure pivot		29.0	0	0
CNMS end part	CuCr1Z	430.3	141.1	786.4
CMS end part		373.3	804.3	702.7
Mirror reflecting surface		119.0	0	0
Rotor	Steel 660	473.0	0	0
CNMS cylindrical part		107.5	252.5	1561.0
CMS cylindrical part		193.4	1439.1	2001.8
Inlet cooling coil	SS316LN	121.7	7581.0	2580.2
Outlet cooling coil		117.6	7324.5	2492.9
Mirror's back plate		687.9	0	1012.2

The analysis setup is divided in 6 sequential load steps. This strategy not only aims at facilitating the numerical convergence, but also to assess the relative contribution of each load step. Table 2 summarizes all steps applied for the NO scenario calculation.

Load step	Fixed support	Gravity (m/s^2)	IBED-PHTS cooling pressure (MPa)	He pressure (MPa)	IBED-PHTS $T_{cooling}$(°C)	Temp. field	Rotation at ±7°
1	ON	9.8066	OFF	OFF	OFF	OFF	0
2	ON	9.8066	4.4	2	OFF	OFF	0
3	ON	9.8066	4.4	2	75	ON	-7
4	ON	9.8066	4.4	2	75	ON	+7
5	ON	9.8066	4.4	2	75	ON	0

Table 2: Load application according to the time steps.

3.1.3. Results

Hydraulic results

The pressure drop is calculated equal to 498.2 kPa while the maximum allowable value for the USMA is 1222.27 kPa. The temperature at the outlet is equal to 113.2 °C. The water velocity is shown in Fig. 8.

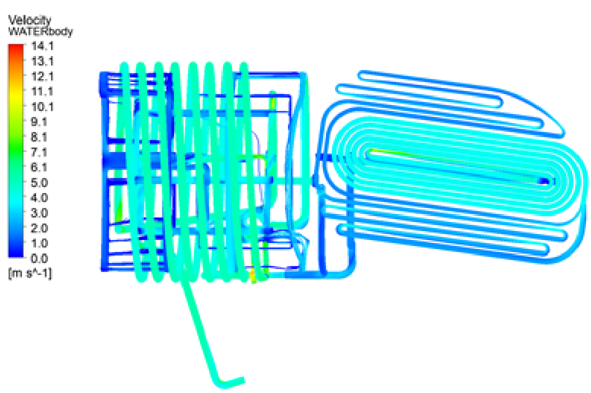

Figure 8: Water velocity of the USMA.

Thermal results

The temperature results of the USMA are shown in Fig. 9. Fig. 10 presents in more detail the temperature results on the inner cooled components like stator and rotor. Fig. 11 presents the temperature

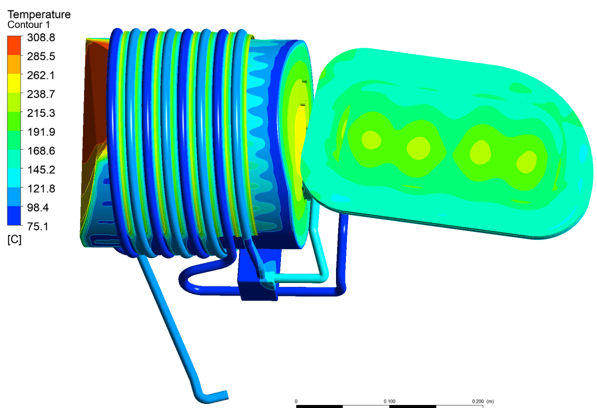

Figure 9: Temperature results of the USMA.

results on the passively components, flexure pivots and bellows. It is worth mentioning the flexure pivots were considered as perfect cylinders in full contact, increasing this way the conduction path between them and the rotor and stator.

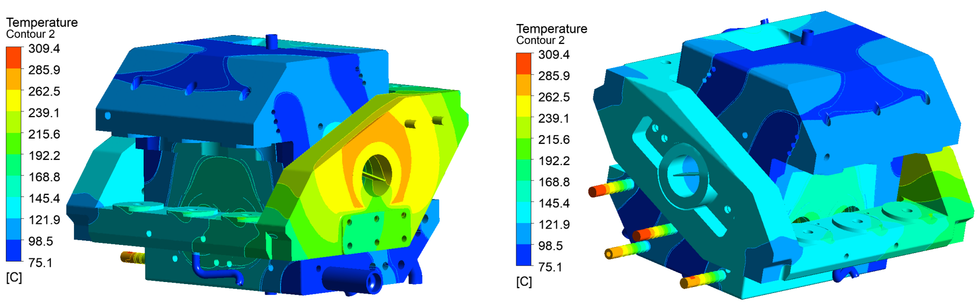

(a) Stator, bellows, rotor and flexure pivots, mirror side.

(b) Stator, bellows, rotor and flexure pivots, non mirror side.

Figure 10: Temperature results of the inner components of USMA, stator, rotor, flexure pivot and bellows.

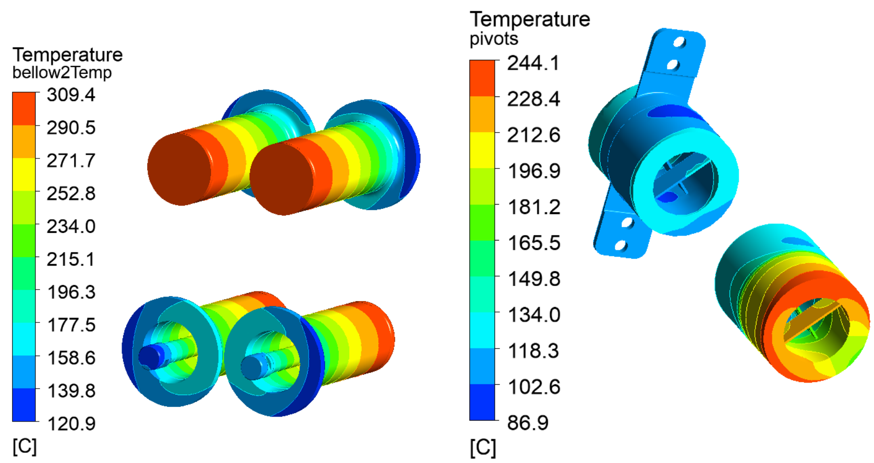

(a) Temperature results on the bellows with a simplified geometry.

(b) Temperature results of the pivots.

Figure 11: Temperature results of the passively components.

Concerning the springs, radiation is not considered in the thermal-hydraulic model but separately. One spring was examined in the steady-state of the thermal module of ANSYS. Nuclear heating was applied volumetrically, the result temperature of rotor and stator was applied, on the two extreme faces which are in contact with stator and rotor. Radiation was assumed in all other faces. The view factor is considered equal to 1. Emissivity values from 0.03 to 1 are considered. After validating the simulation results, analytically, different view factors (0.1 to 1) were considered.

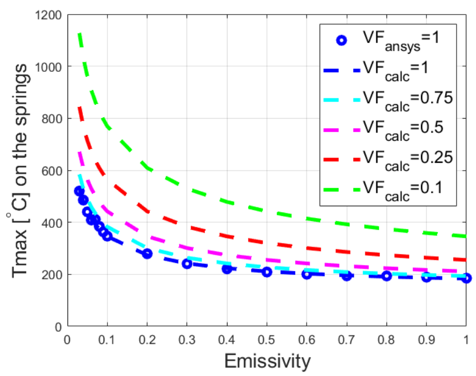

Figure 12: Maximum temperature on the springs surface versus emissivity for various view factor values.

Stress results - structural integrity assessment

Figs. 13, 14 present the final stress state of the protective covers as well as the rest of the USMA components. This includes Primary (P) and Secondary (Q) stresses. In order to assess the stress integrity of the in-vessel components during the NO scenario, against plastic collapse and ratcheting, the stresses are computed and classified into categories according to the ITER SDC-IC code. The stress categorization is obtained by linearizing the stress (membrane, bending and peak) along the so-called Stress Classification Lines (SCLs). SCLs (Fig. 24) are generated at the regions of the highest stresses in the most critical components like rotor, mirrors assembly, protective covers, cooling coils and flexure pivots in order to decouple P and Q stresses. The stress intensity is extracted from the SCLs and the results are compared with the material limits given in the Appendix A of SDC-IC [5]. Table 7 in the Appendix 7 presents the categorized stress results of the examined components with the allowable design limits [5] for each material at the maximum reached temperature. The comparison between them shows that the USMA assembly design is capable of withstanding (in terms of plastic collapse and ratcheting) the expected loads taking place during the normal mm-wave operation scenario.

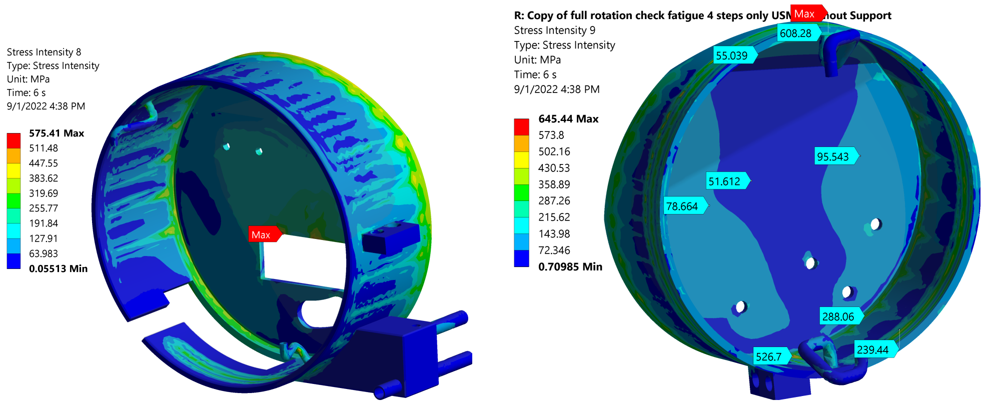

(a) Stress intensity results (MPa) on the cap which is fixed to the rotor.

(b) Stress intensity results (MPa) on the cap which is fixed to the stator.

Figure 13: Stress intensity results on the protective covers.

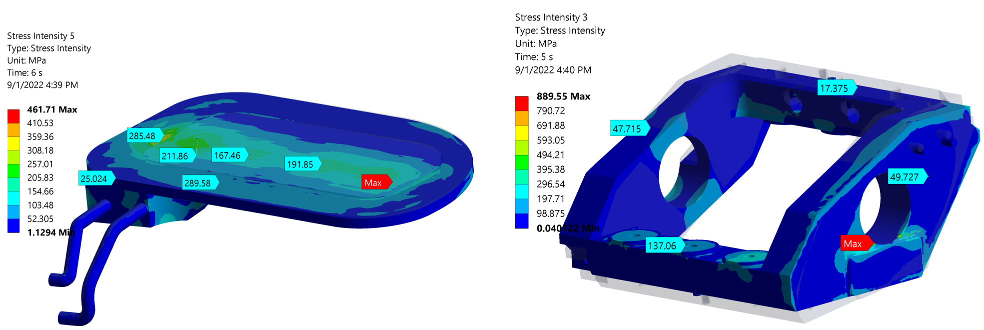

(a) Stress intensity results (MPa) on the mirror assembly.

(b) Stress intensity results (MPa) on the rotor.

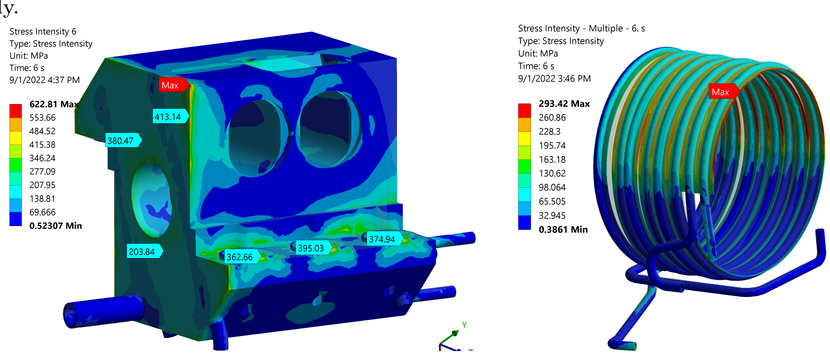

(c) Stress intensity results (MPa) on the stator.

(d) Stress intensity results (MPa) on the cooling coils.

Figure 14: Stress intensity results of the USMA.

Fatigue

During ITER lifetime, the SMA will experience cyclic loading that could compromise its mechanical integrity. The number of fatigue cycles to be considered is $60 \cdot 10^3$ rotations at full steering mirror range.

Fig. 15 presents the stress intensity of the flexure pivots on the mirror side and the non-mirror side. The pivots are made of Alloy 718. Both rotation angles give similar stress results, here for simplicity one position is presented. Numerical singularities appear at the sharp corners of the cells. Considering that the pivots rotate from -7° to +7°, (fully reversed cycle R=-1), the S_a=530 MPa for flexure pivot mirror side and S_a=600 MPa for the flexure pivot non-mirror side. This value exceeds the upper limit of Alloy 718, which is 328 MPa for $60 \cdot 10^3$ cycles [5].

Fig. 16 presents the stress intensity results of pivots using Ti6Al-4V alloy instead of Alloy 718. In this case the S_a=380 MPa for the flexure pivot on the mirror side, whereas it is 300 MPa on the flexure pivot on the non-mirror side. According to the Military Handbook [8] the allowable for $60 \cdot 10^3$ cycles is 687.5 MPa. The comparison of the S-N data for both materials is shown in Fig. 17.

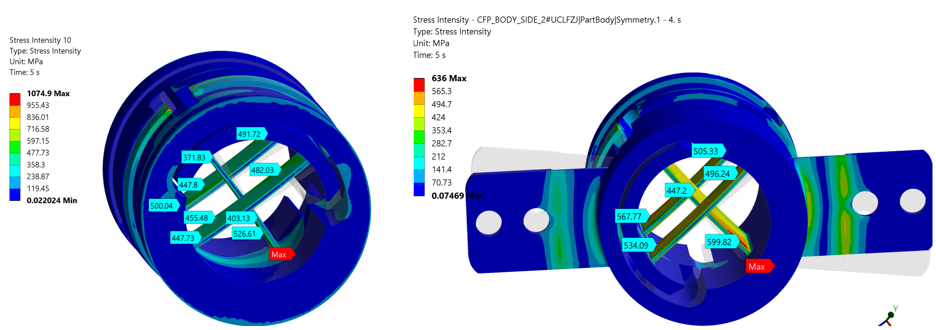

(a) Flexure pivot (Alloy718) on the mirror side.

(b) Flexure pivot (Alloy718) on the non mirror side.

Figure 15: Stress intensity results on the flexure pivots made of Alloy 718.

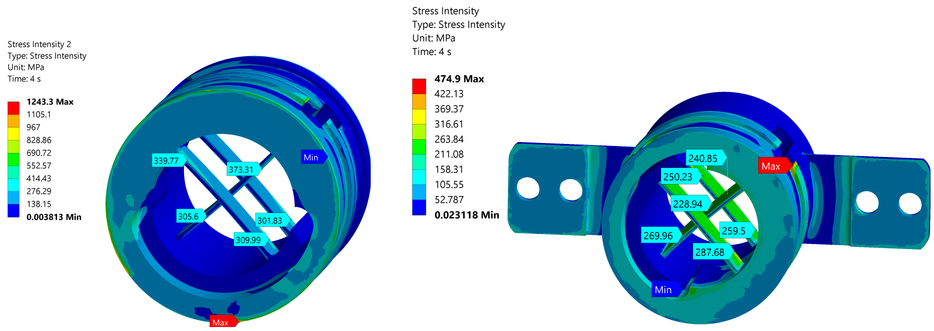

(a) Flexure pivot (Ti6Al-4V Alloy) on the mirror side.

(b) Flexure pivot (Ti6Al-4V Alloy) on the non mirror side.

Figure 16: Stress intensity results on the flexure pivots made of Ti6Al-4V alloy.

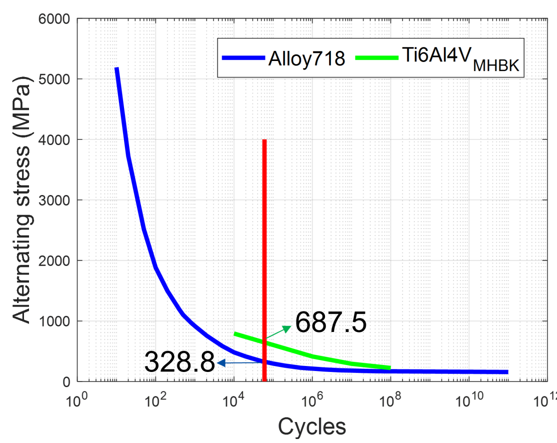

Figure 17: S-N curves for the fatigue properties of Alloy 718 [5] and Ti6Al4V [8].

3.2. VDEIII

3.2.1. Geometry-Excitations

The USMA is considered in the VDEIII analysis Fig. 18. The stator as well as the springs and the bellows are not modelled. The cooling channels in the protective covers and the rotor have been suppressed for computational efficiency.

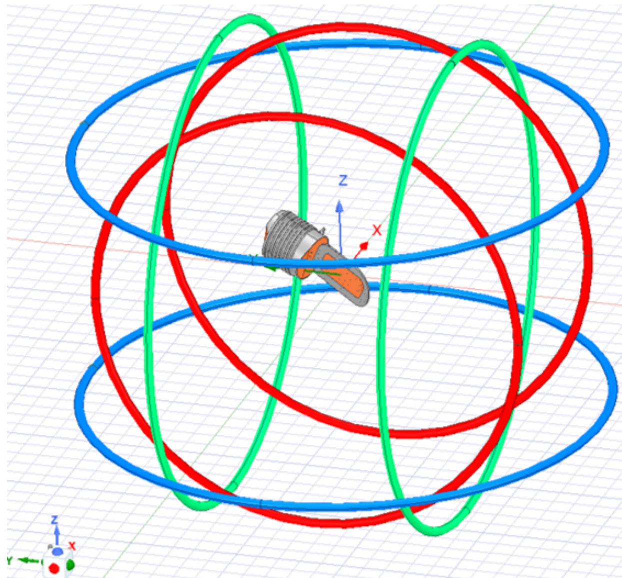

Figure 18: Geometry used for the EM analysis. The USMA is considered in the center of the Helmholtz coils. The coils reproduce the magnetic field on the x, y and z axis; here are shown with salmon, green and blue color, respectively. The vacuum volume has diameter equal to 4m and it covers all shown items.

The material properties used for the electromagnetic analysis are extracted from the ITER Material Handbook (Table 3).

Two analyses are performed. One examines the covers with combination of materials (CuCr1Zr for the end part and steel 660 for the cylindrical part) and on the other analysis Alloy 660 is considered in the whole volume of the protective covers.

Table 3: Electrical Conductivity of the metals, recommended values for room temperature.

Electrical conductivity	S/m
CuCr1Z alloy	46000000
316L(N)-IG	1330000
Steel Grade 660	1100000
Alloy 718	1187000

Since the global Electromagnetic model including the latest design is not available, the Helmholtz-coils approach is used to calculate the induced forces and moments for the two material cases. Three orthogonal pairs of Helmholtz coils are modelled in order to obtain the three time transient components of the magnetic field [9]. To avoid the geometrical interference among them, a different radius is used for each couple of Helmholtz coils. Radius of 1, 1.1 and 1.2 m are used for the Helmholtz coils generating B_x, B_y and B_z fields, respectively. The $\Delta B/\Delta t$ time variation is shown in Fig. 19a). From this the equivalent currents are calculated using Eq. 1 (Fig. 19b). The calculated currents are applied to the terminals defined in the coils. This strategy is used since the direct application of a time-dependent magnetic field is not implemented in ANSYS Maxwell. Vacuum volume is considered in a sphere with a diameter equal to 4 m which encapsulates all the SMA components as well as the coils (see Fig. 18 left side). The times steps for the problem resolution are variable allowing to accurately trace the magnetic field variation provided by the source. The simulation finishes at t = 0.8709 s, time at which the last source value is provided.

$$\overrightarrow{B} = \frac{\mu_0 I}{(5/4)^{(3/2)} a} \tag{1}$$

where $\overrightarrow{B}|_{z=0}$ is the magnetic field at the centre of the Helmholtz coils, I is the current (in Amperes) passing through each coil (in a single turn), a is the coil radius (in meters) (as well as the distance between them) and $\mu_0 = 4\pi 10^{-7}$ Hm^{-1} is the permeability of the free space.

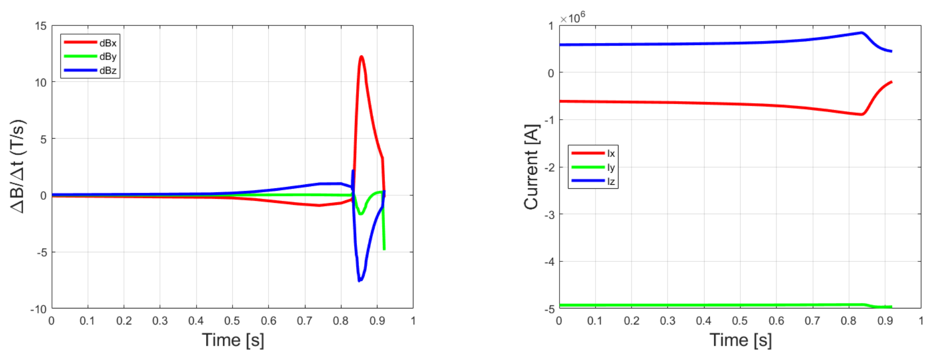

(a) ΔB/ΔT time history for the USMA.

(b) Current values for x, y and z direction.

Figure 19: Time history of the ΔB/ΔT on the left and of the currents on the right for the USMA.

3.2.2. Results

Fig. 20a shows the induced current at t = 0.87 s (moment of the peak in ΔB/ΔT) in the USMA components. As shown in Fig. 19a, the largest magnetic field variations (ΔB/Δt) are along the radial and vertical axis (x and z axis). These variations induce a current density, especially the radial one since this magnetic field component is almost perpendicular to the USMA. The maximum current density value induced in the USMA is 2.6e7 A/m^2 (on the mirror surface).

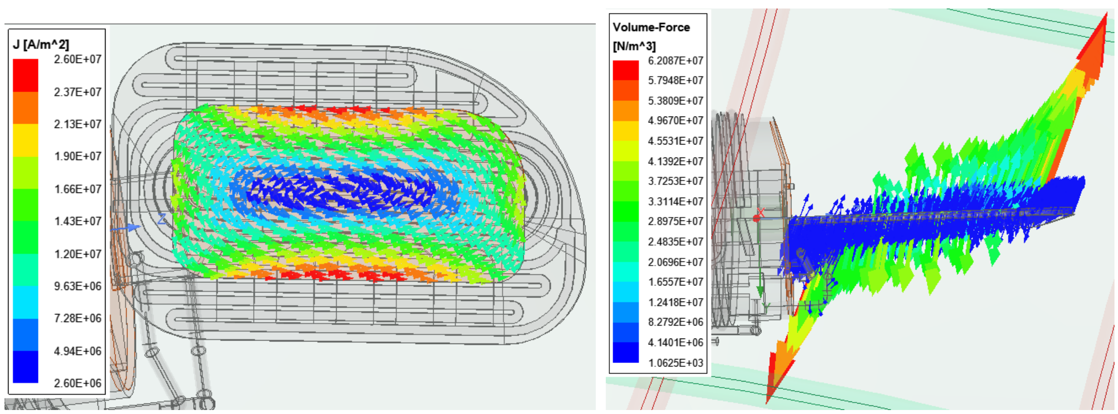

(a) Current density (A/m^2).

(b) Force density (N/m^3).

Figure 20: Current and force density extracted at the mirror for the time instant t = 0.87 s, in the central copper region. The racetrack shaped outer region of the mirror is composed of stainless steel and thus conducts only marginally induced currents.

Fig. 20b shows the volumetric forces at t = 0.87 s induced the reflecting surface of the mirror.

A local coordinate system is placed in the center of the flexure pivot mirror side. The induced moments and forces are extracted relevant to this coordinate system for the pivots. Both material cases (combination of CuCr1Zr-Alloy 660 and uniform Alloy 660) are considered for the protective covers, Fig. 21 presents this comparison.

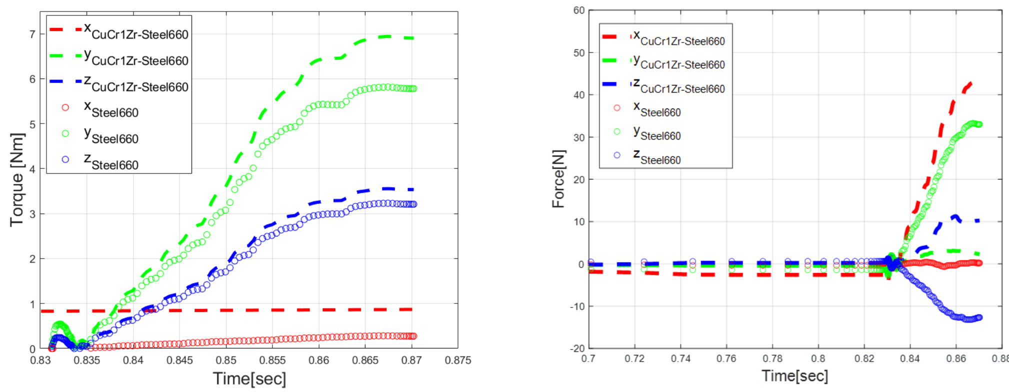

(a) Induced moments (Nm).

(b) Induced forces (N).

Figure 21: Induced moments and forces on the pivots extracted from a local coordinate system at the center of pivot mirror side. The two cases with CuCrZr1 and Alloy 660 on the flat parts are compared.

4. Discussion and Conclusions

The results of the thermal-hydraulic analyses prove that the introduction of cooled protective covers has negligible effects on the overall pressure drop, water velocity and temperature characterizing the active cooling of the assembly. Considering conservative loads of plasma heating while assuming complete stray radiation screening from the covers and the coils, the presented results show that the thermal performance of the inner uncooled components (flexure pivots, bellows and springs) has been considerably improved. However, full stray radiation shielding has yet to be demonstrated. Also, an update of the plasma heating distribution and the nuclear loads calculation, considering the revised M4 design will be needed.

The comparison between the stress intensity on the several components and the material limits at the maximum temperatures shows that the USMA assembly design withstands (in terms of plastic collapse and ratcheting) the expected loads taking place during the NO scenario. After ensuring the NO scenario, this should be combined with seismic load and VDE loads in order to further validate the design. Concerning the protective covers, if the channels remain as they are currently, a material with equivalent strength as the Alloy 660 needs to be used in order to withstand the primary stress generated by the water pressure. Otherwise, in order to use a material like stainless steel 316LN, the channels need to be reduced in width and the pressure drop to be revisited. It is worth mentioning that if the additive manufacturing of the covers could be allowed, narrow uniform channels could be integrated in the whole volume of the covers with uniform material.

The fatigue check on the pivots showed that the pivots made of Alloy 718 can not sustain the required angular cycles ($60 \cdot 10^3$) of the NO scenario. By repeating the same exercise with Ti6Al4V alloy as pivot material, the resulting stresses are lower and the pivots can sustain the $60 \cdot 10^3$ cycles according to the Military Handbook [8] (maximum allowable for the 60e3 cycles is 687.5 MPa).

The Electromagnetic (EM) analysis of the VDEIII case performed here only to compare the effect of the two different materials (Alloy 660 with CuCr1Zr and uniform Alloy 660) in the induced moments and forces. The results showed that the effect generated by the flat parts of the covers in CuCr1Zr is not significant. Since the induced moments and forces in this case are only slightly higher compared to the case that the covers are uniformly made of Alloy 660. A classic EM analysis shall be performed with the global model in order to extract accurately the induced forces and moments needed for the calculating additional load cases in the mechanical solver.

5. Acknowledgements

This work was supported in part by the Swiss National Science Foundation. This work was carried out within the framework of the F4E contract F4E-OFC-0958. The views and opinions expressed herein do not necessarily reflect those of the European Commission or the ITER Organization.

References

[1] R. Chavan, M. Henderson, F. Sanchez, A frictionless steering mechanism for the front steering eccd iter upper port launcher, in: Journal of Physics: Conference Series, Vol. 25, IOP Publishing, 2005, p. 019.

[2] P. Santos Silva, R. Chavan, T. Goodman, A. Mas Sánchez, M. Vagnoni, Design and thermal-structural analyses of ancillary components for the optical steering mirror (m4) for the iter ech upper launcher, IEEE Transactions on Plasma Science 48 (6) (2020) 1525–1530. doi:10.1109/TPS.2020.2974545.

[3] M. Vagnoni, R. Chavan, T. Goodman, A. Xydou, Design optimization of the upper steering mirror assembly (usma) for iter echul in view of disruptive events, Fusion Engineering and Design 167 (2021) 112343. doi:https://doi.org/10.1016/j.fusengdes.2021.112343.
URL https://www.sciencedirect.com/science/article/pii/S0920379621001198

[4] I. ITER, Iter structural design criteria for in-vessel components (sdc-ic) (2012).

[5] R. Atroshenkov, G. Kalinin, V. Barabash, Appendix a, materials design limit data, In-vessel Components, SDC-IC, ITER v3.3.

[6] D. Ronden, M. de Baar, R. Chavan, B. Elzendoorn, G. Grossetti, C. Heemskerk, J. Koning, J.-D. Landis, P. Spaeh, D. Strauss, The iter ec hcd upper launcher: Maintenance concepts, Fusion Engineering and Design 88 (9) (2013) 1982–1986, proceedings of the 27th Symposium On Fusion Technology (SOFT-27); Liège, Belgium, September 24-28, 2012. doi:https://doi.org/10.1016/j.fusengdes.2012.12.031.
URL https://www.sciencedirect.com/science/article/pii/S0920379612005881

[7] V. Barabash, J. Dietz, K. Ioki, G. Janeschitz, G. Kalinin, R. Matera, K. Mohri, Materials aspects of iter in-vessel components, in:

C. VARANDAS, F. SERRA (Eds.), Fusion Technology 1996, Elsevier, Oxford, 1997, pp. 347–350. doi:https://doi.org/10.1016/B978-0-444-82762-3.50057-4.
URL https://www.sciencedirect.com/science/article/pii/B9780444827623500574

[8] U. S. D. of Defense, Military Handbook: Metallic Materials and Elements for Aerospace Vehicle Structures, Vol. 1, US Department of Defense, 1990.

[9] A. Mas Sánchez, R. Chavan, T. Goodman, P. Santos Silva, M. Vagnoni, Electromagnetic and mechanical analyses of the iter electron cyclotron upper launcher steering m4 mirrors for the vertical displacement event, Fusion Engineering and Design 159 (2020) 111941. doi:https://doi.org/10.1016/j.fusengdes.2020.111941.
URL https://www.sciencedirect.com/science/article/pii/S0920379620304890

6. Appendix 1: Thermal loads on the mirrors

6.1. Ohmic dissipation of microwaves at the reflecting surface

Each mirror reflects beams with an incident angle ($\Theta_{inc} = \theta/2$), where θ is the angle between the input and the output beam direction at the mirror. At 170 GHz, the imaged currents (and the absorbed power) concentrate within a thin layer (skin depth) at the surface of the conductor. The skin depth is a function of the mirror material resistivity (for the M4, CuCr1Zr) ρ_e. For the plasma facing components, the surface may deteriorate over time, increasing the surface roughness. To account for this effect, the surface factor “S” (capital case) is used. For example, S = 2.2 is assumed for UM4/LM4.

The fractional lost power is calculated for each beam depending on its incident angle and polarization. The required polarization of the beam changes with the angle of injection from the last mirror (M3) and is slightly different for each beam. For E-plane polarized waves (electric field vector lies on the plane formed by the normal to the reflecting surface and wave-vector of the incident radiation) the fractional lost power, $f_{\Omega E}$, is given by Equation 2. This is the worst-case power loss fraction.

$$f_{\Omega E} = 4 \cdot S_{\text{eff}} \sqrt{\frac{\pi \cdot \rho_e}{\lambda \cdot Z_0}} \cdot \frac{1}{cos\frac{\theta}{2}} \tag{2}$$

Where:

- S_{eff} is a surface factor that takes into consideration the surface roughness, micro-cracks, impurities, etc. In the current case the s is taken equal to 2.2.
- ρ_e is the temperature dependent electrical resistivity of the facing component. In our case the Mirror Material is CuCr1Z, with ρ_e equal to:

$$\rho_e = 6.76e^{-11} \cdot T + 2.03e^{-8}[Ohm \cdot m/K] \tag{3}$$

- Z_0 is the impedance of the free space ($\sqrt{\frac{\mu_0}{\epsilon_0}} = c \cdot \mu_0 \approx 120 \cdot pi$)
- λ is the wavelength at 170 GHz.

The angles $\theta_{(1-4)}$ are described in Table 4. With the absorbed fraction the heat flux per single beam can be calculated as shown in Equation 4. In general, for astigmatic beams, the size of the beam differs in the two orthogonal planes x-z and y-z. For non-astigmatic (circular) beams the x and y components of the spot sizes are equal.

$$q"_i(x,y,\theta) = \frac{(2P_0 f_{\Omega i} cos(\theta_i/2))}{(\pi\omega_{mxi} w_{myi})} \cdot exp(-2(\frac{(x-x_i)^2}{(\omega_{mxi})^2} + \frac{(y-y_i)^2 cos^2\theta_i/2}{(w_{myi})^2})) \quad (4)$$

The UM4 and LM4 reflect four beams. Therefore, the total heat flux is given in Equation 5.

$$q"_{TOT}(x,y,\theta) = q"_1 + q"_2 + q"_3 + q"_4 [MW/m^2] \quad (5)$$

Where:

- i is the index of the beams.
- P_0 is the input power equal to 1.08 MW.
- cos(θ/2) in the numerators of fractions comes from the fact that the beam waist is elongated in the y-direction by a factor 1/cos(θ2) – that is, the plane of reflection defines the y-direction.
- ω_{mx} is the specific beam spot size for each beam in the x-direction.
- ω_{my} is the specific beam spot size for each beam in the y-direction.
- x_i, y_i are the coordinates of the center of the beam spot from the local axis system.

Eq. 4 and 5 apply to both UM4 and LM4. On M4, the beam is astigmatic so the so-called poloidal and toroidal spot sizes must be used. In the ITER Upper Launcher, the poloidal direction corresponds most closely to the y-direction and the toroidal direction most closely to the x-direction.

By using Eq. 4 and 5 as well as the parameters in Table 4 the Ohmic losses in both mirrors are derived for both rotation angles as shown in Fig. 22. The maximum values are summarized in Table 5.

Table 4: Parameters used to calculate the Ohmic losses on the USMA and LSMA.

Parameters	LM4 (-7°)	LM4 (+7°)	UM4 (-7°)	UM4 (+7°)
wmx1	129.4	128.7	122.6	123.5
wmx2	129.9	129.4	122.3	123.2
wmx3	130.6	130.3	122.4	123.1
wmx4	131.3	131.2	122.5	122.9
wmy1	143	164	167.3	199
wmy2	143.1	163.6	166.6	196.4
wmy3	143.2	163.2	166.1	194.7
wmy4	143.2	162.5	165.4	192.5
xb1	76.2	76.3	86.9	83.63
xb2	25.2	25.3	31	30.17
xb3	-26.4	-26.4	-31.4	-30.48
xb4	-72.8	-72.8	-87.8	-84.89
yb1	5.5	6.3	-13.9	-29.57
yb2	2.5	2.8	-2.9	-8.16
yb3	-4.1	-4.6	3.5	8.88
yb4	-10.5	-11.9	13.5	29.11
θ01	48.09	73.82	62.36	88.28
θ02	46.69	72.54	60.65	86.44
θ03	45.12	71.05	59.4	85.03
θ04	43.15	69.13	57.91	83.31

Table 5: Peak values of the Ohmic heating (W/m^2).

	Maximum Ohmic heating (W/m^2)
UM4H	1.38e6
UM4L	1.45e6
LM4H	1.61e6
LM4L	1.62e6

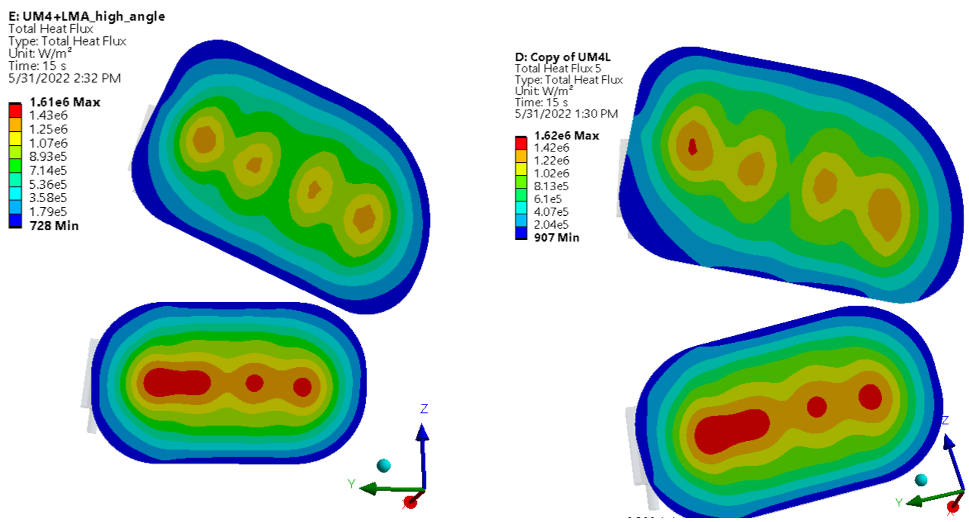

(a) Rotation angle of -7°.

(b) Rotation angle of +7°.

Figure 22: Ohmic losses on Upper and Lower mirror at rotation of ±7°.

6.2. Plasma heating

The plasma radiation has been calculated for a simplified design of the SMA. This model had neither the protective covers, nor the cooling coils and springs (Fig. 23). The mapping of this available data on the current design would lead to inaccurate result. Therefore, since a radiation map on the current design is not available, as a conservative approach the uniform value of $57\,\mathrm{kW/m^2}$ in the faces of the mostly exposed to plasma components, like the protective covers fixed to the rotor, the cooling coils and mirror's reflective surfaces. This is assumed considering their approximate position relative with radiation maps given in Fig. 23. On the cover which is fixed to the stator it was decided to use $10\,\mathrm{kW/m^2}$ since according to this map the heat flux applied to this side is the minimum.

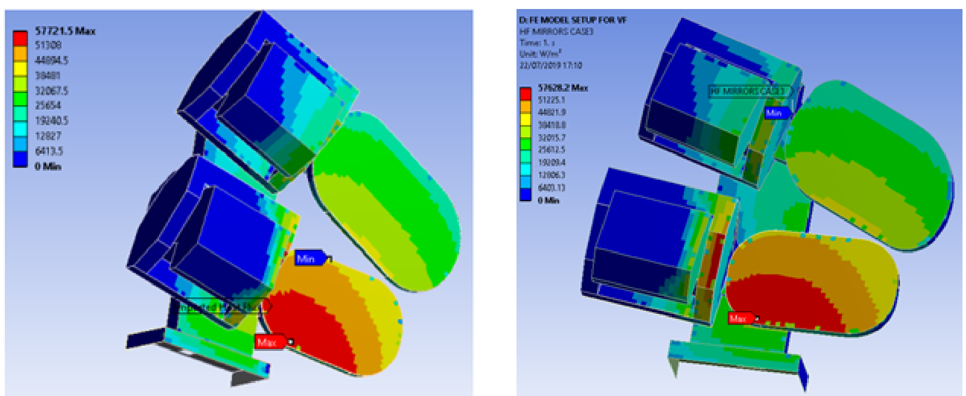

(a) Plasma heating view from the non mirror side. (b) Plasma heating view from the mirror side.

Figure 23: Resulting plasma heating ($\mathrm{W/m^2}$) distribution over the simplified SMA.

6.3. Nuclear heating

The neutronic analysis had been performed in the past with the previous design of the SMA (without the protective covers). In the meantime the design had been evolved and the material properties of some components had been changed. In this analysis the total nuclear heating is given as a sum of heating by neutrons and heating by prompt photons in Watts per group of components with the same material. A summary is shown below in Table 6. As shown in the list of components and materials, the material properties of pivots and springs is not currently valid. In addition, the covers were not present in this analysis.

Therefore, to apply the neutronic heating to all components, the approach of best estimate was applied. By taking the ratio of the volumes and multiply with the available power level per material given in Table 6.

$$NH = \frac{Volume_{component}}{Volume_{total}} \cdot NH_{total} \tag{6}$$

Table 6: Nuclear heating in the SMA components.

Nuclear heating	W	Total volume (m^3)
CuCr1Zr (Mirrors)	235	1.03E-04
XM19 (Support and stators)	3338	8.03E-03
Alloy X-750 [1] (springs)	336	6.18E-04
Ti6Al4V (pivots)	63.8	2.39E-04
Inconel 718 (bellows)	141	2.94E-04
Alloy 660 (rotors)	946	1.82E-03
SS316LN (coils and mirror supports)	1458.9	1.59E-03

7. Appendix 3: Classification lines

Table 7: Stress intensity values in MPa extracted from the SLCs of the listed components, compared with the materials limits at the highest temperature.

Component	SLCs	1	2	3	4	5	6	7	8	9	10	Limit @250°C
Rotor	P_m	20.7	29.2	24.2	15.5	9.2	6.5	6.9	40.3	28.0	27.1	292.0
	$P_l + P_b$	25.2	55.3	33.4	49.6	31.4	13.7	26.9	73.3	51.7	54.3	438.0
	$P_l + P_b + Q$	97.0	84.0	35.3	35.7	43.9	17.6	25.9	160.9	105.8	92.0	876.0
	SLCs	1	2	3	4	5	6	7	8	9	10	Limit @222°C
mirrors support	P_m	6.6	7.8	5.2	6.2	11.9	6.6	7.6	5.3	8.4	6.3	125.0
	$P_l + P_b$	9.5	15.9	8.7	8.9	26.3	10.0	15.0	6.3	17.5	12.9	187.5
	$P_l + P_b + Q$	217.6	130.9	165.2	157.1	214.9	145.8	281.2	250.9	275.5	154.4	375.0
	SLCs	1	2	3	4	5	6	7	8	9	10	Limit @224°C
mirrors ref surface	P_m	3.4	6.7	4.3	5.5	5.1	7.9	8.7	6.3	6.6	7.9	103.0
	$P_l + P_b$	5.3	8.6	8.1	5.9	6.3	13.1	17.1	8.8	8.9	17.0	154.5
	$P_l + P_b + Q$	273.6	214.0	221.9	259.2	263.5	248.3	270.1	256.3	199.5	225.0	309.0
	SLCs	1	2	3	4	5	6	7	8	9	10	Limit @125°C
flexure pivot NMS	P_m	64.3	62.7	81.5	64.3	130.7	130.2	68.2	57.6	117.8	87.4	414.0
	$P_l + P_b$	63.5	61.2	81.8	64.2	135.4	124.2	69.1	57.4	117.0	87.8	621.0
	$P_l + P_b + Q$	442.3	446.4	470.4	415.9	501.6	559.1	388.1	386.1	529.0	363.9	1242.0

	SLCs	1	2	3	4	5	6	7	8	9	10	Limit @245°C
flexure pivot MS	P_m	34.4	18.5	50.3	5.0	75.1	49.0	101.8	12.1	40.8	22.6	414.0
	$P_l + P_b$	29.4	13.5	56.0	14.9	85.5	46.4	95.5	1.4	28.6	33.3	621.0
	$P_l + P_b+Q$	490.8	442.4	519.1	379.9	510.5	427.1	536.6	449.9	499.4	447.5	1242.0
	SLCs	1	2	3	4	5	6	7	8	9	10	Limit @180°C
cap MS	P_m	122.8	35.2	175.3	76.2	38.8	1.4	59.2	122.3	0.9	172.3	299.0
	$P_l + P_b$	122.4	35.3	173.6	75.1	38.5	7.7	58.4	120.2	7.0	170.8	448.5
	$P_l + P_b+Q$	407.7	326.2	394.5	363.4	58.5	79.9	299.2	86.7	48.1	169.9	897.0
	SLCs	1	2	3	4	5	6	7	8	9	10	Limit @306°C
cap NMS	P_m	154.6	241.8	139.0	111.2	29.8	15.3	203.6	137.9	136.2	64.1	292.0
	$P_l + P_b$	127.5	376.0	228.1	170.7	29.0	13.7	397.3	242.4	296.1	63.7	438.0
	$P_l + P_b+Q$	280.0	554.0	332.5	211.3	50.5	87.9	529.0	318.0	363.5	32.4	876.0
	SLCs	1	2	3	4	5	6	7	8	9	10	Limit @205°C
Inlet coil	P_m	13.9	47.2	31.0	15.4	13.7	16.3	14.5				125.0
	$P_l + P_b$	17.1	46.7	54.9	15.9	17.5	16.4	16.3				187.5
	$P_l + P_b+Q$	77.8	57.4	9.6	86.0	81.0	77.2	17.6				375.0
	SLCs	1	2	3	4	5	6	7	8	9	10	Limit @234°C
Outlet coil	P_m	45.8	34.5	29.2	12.8	18.3	46.0	21.5				121.0
	$P_l + P_b$	45.8	35.2	39.3	17.9	18.3	46.5	23.3				181.5
	$P_l + P_b+Q$	28.2	15.1	23.9	39.5	52.2	39.5	39.1				363.0

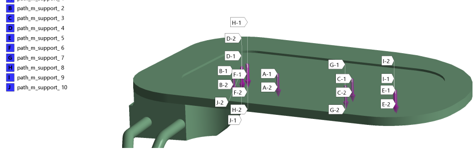

(a) SLCs on the mirror support.

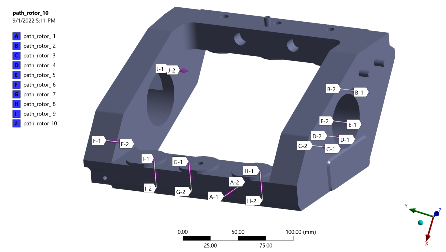

(b) SLCs on the mirror support on the rotor.

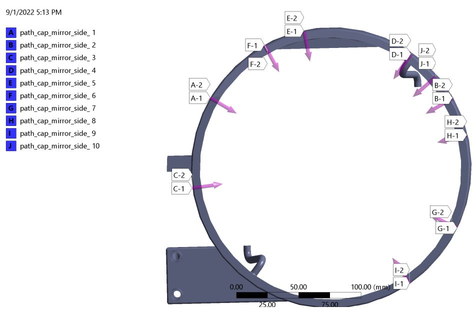

(c) SLCs on the caps fixed to the rotor.

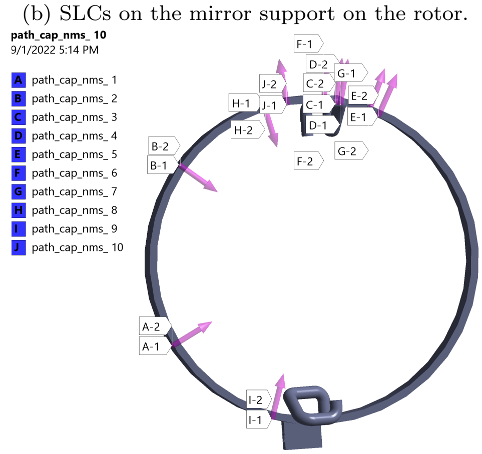

(d) SLCs on the caps fixed to the stator.

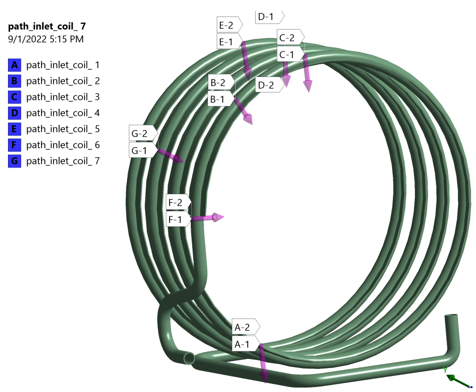

(e) SLCs on the inlet cooling coil.

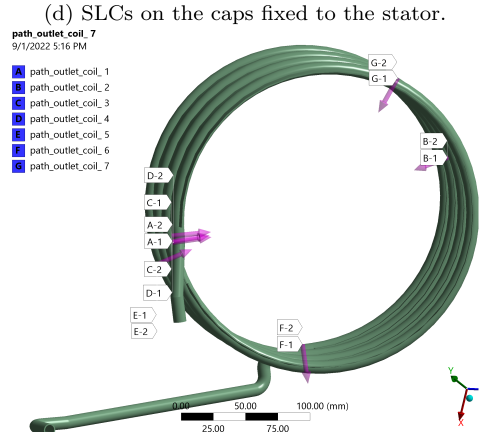

(f) SLCs on the outlet cooling coil.

Figure 24: Classification lines are employed in the regions of the maximum stress intensity.

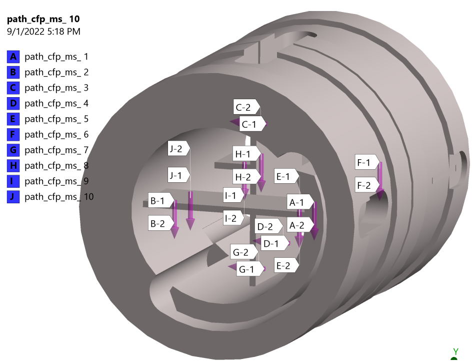

(a) SLCs on the flexure pivot of the mirror side.

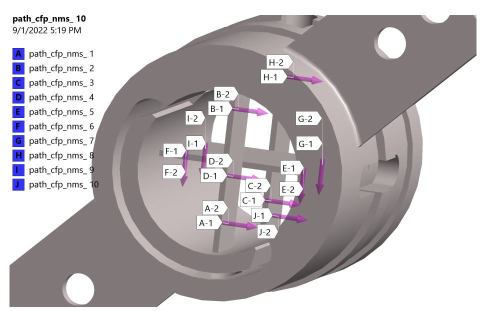

(b) SLCs on the flexure pivot of the non mirror side

Figure 25: Classification lines are employed on the blades of both pivots at the regions where high stress intensity appears.